JGR Space Physics

RESEARCH ARTICLE
10.1029/2018JA026222

The Effect of Fast Normal Mode Structure and Magnetopause Forcing on FLRs in a 3-D Waveguide

T. Elsden[1] **and A. N. Wright**[1]

[1]Department of Mathematics and Statistics, University of St Andrews, St Andrews, UK

Key Points:
- Waveguide normal mode structure is determined by the equilibrium
- Structure of waveguide normal modes is key in determining coupling efficiency and resonance location
- Magnetopause driver determines which normal modes are excited and hence the FLR locations

Supporting Information:
- Supporting Information S1
- Movie S1

Correspondence to:
T. Elsden,
te55@st-andrews.ac.uk

Citation:
Elsden, T., & Wright, A. N. (2019). The effect of fast normal mode structure and magnetopause forcing on FLRs in a 3-D waveguide. *Journal of Geophysical Research: Space Physics*, *124*. https://doi.org/10.1029/2018JA026222

Received 22 OCT 2018
Accepted 6 DEC 2018
Accepted article online 15 DEC 2018

Abstract This paper investigates the excitation of waveguide modes in a nonuniform dipole equilibrium and, further, their coupling to field line resonances (FLRs). Waveguide modes are fast compressional ultralow frequency (ULF) waves, whose structure depends upon the magnetospheric equilibrium and the solar wind driving conditions. Using magnetohydrodynamic simulations, we consider how the structure of the excited waveguide mode is affected by various forms of magnetopause driving. We find that the waveguide supports a set of normal modes that are determined by the equilibrium. However, the particular normal modes that are excited are determined by the structure of the magnetopause driver. A full understanding of the spatial structure of the normal modes is required in order to predict where coupling to FLRs will occur. We show that symmetric pressure driving about the noon meridian can excite normal modes which remain around to drive resonances for longer than antisymmetric driving. Further, the critical quantity in terms of efficient coupling is the magnetic pressure gradient aligned with the resonance.

Plain Language Summary Earth's magnetic field is constantly being disturbed by the outflow from the Sun (the solar wind). Such disturbances generate periodic oscillations of the Earth's magnetic field, which can be measured by instruments on the ground and in space. These oscillations (waves) have been shown to have an impact on the aurora and the motion of energetic particles within the radiation belts (regions of trapped energetic particles around the Earth). In this study, we use a computational model of the Earth's magnetic field to investigate how these waves propagate. We consider various ways of driving the system, together with different density distributions and measure the resulting wave response. We identify that the system supports what are called "fast normal modes," which are the natural waves of the system. These can be thought of in the same way as blowing across an open bottle, which will produce a specific frequency of sound. We discuss how the structure of these modes affects how energy propagates and accumulates throughout the Earth's magnetic environment.

1. Introduction

The propagation of fast magnetohydrodynamic (MHD) waves in the outer magnetosphere has been studied extensively. Fast waves are compressive and propagate across the magnetic field, meaning that they communicate global changes in the magnetospheric equilibrium due to driving by the solar wind. There are a variety of models that have been used to study such wave modes, which manifest in the magnetosphere as ultralow frequency (ULF) waves (frequencies 1 mHz to 1 Hz; Jacobs et al., 1964). The cavity model (Allan et al., 1985, 1986; Kivelson & Southwood, 1985, 1986; Leonovich & Mazur, 2000, 2001) treats the outer magnetosphere as an axisymmetric closed cavity, where fast mode waves can have a radially standing mode structure between different magnetospheric boundaries, for example, between the plasmapause, magnetopause, or a turning point. The cavity supports a discrete set of normal modes since the azimuthal wavenumber is, by the nature of the closed system, quantized. This is well elucidated in simulations presented by Wright and Rickard (1995), where a cavity is driven with a solar wind-like broadband spectrum. The cavity responds with its fast normal modes, producing an incredibly monochromatic response in the cavity interior. Such fast modes can couple to the transverse, incompressible Alfvén mode, through a process known in Earth's magnetosphere as field line resonance (FLR; Chen & Hasegawa, 1974; Southwood, 1974). In the cavity model, the discrete frequency cavity modes drive FLRs at the location where the local toroidal Alfvén frequency matches this

©2018. American Geophysical Union. All Rights Reserved.

cavity frequency (e.g., Allan et al., 1986; Inhester, 1987; Kivelson & Southwood, 1986; Klimushkin et al., 2004; Lee & Lysak, 1989, 1990; Leonovich & Mazur, 1989; Leonovich, 2001) and are toroidal in nature.

Modeling the magnetosphere as an open-ended waveguide rather than a closed cavity allows for normal modes with a continuous spectrum of azimuthal wavenumbers (Harrold & Samson, 1992; Mazur & Chuiko, 2015; Rickard & Wright, 1994; Samson et al., 1992; Walker et al., 1992). The propagation of fast modes in a Cartesian waveguide with nonuniformity only in the radial direction was studied by Wright (1994). Through ray trajectories, this study argued that the waveguide modes which most efficiently drive FLRs have a small k_y, where k_y is the azimuthal wavenumber, since they remain at a given azimuthal location for longer than modes with a larger k_y. Observationally, there are many previous studies which give credence to the treatment of the magnetosphere as a waveguide (Eriksson et al., 2006; M. Hartinger et al., 2012; M. D. Hartinger et al., 2013; Rae et al., 2005). It has been noted that cavity and waveguide modes can be difficult to detect in satellite data for various reasons, such as obscuring by other ULF wave modes and not having the appropriate radial placement of satellites to properly identify such modes (Hartinger et al., 2014).

In this work, we are interested in the structure of fast waveguide modes and how their structure affects the FLRs that they drive, particularly in a 3-D inhomogeneous magnetospheric equilibrium. Understanding the structure of the fast mode which develops in an asymmetric equilibrium about noon has been used recently to explain the dawn-dusk asymmetry of Pc5 wave observations (Wright et al., 2018). Further, the inclusion of azimuthal magnetic and density asymmetries has also been used to consider the effect of a plasmaspheric plume on ULF wave propagation (Degeling et al., 2018). A key aspect of the current work is considering the excitation of FLRs in 3-D (Elsden & Wright, 2017, 2018; Wright & Elsden, 2016), where resonances can exist at any given polarization angle between toroidal and poloidal. Elsden and Wright (2017) showed that the important quantity for efficient resonant excitation is the magnetic pressure gradient along the direction of polarization of the Alfvén wave. Hence, it is critical to understand the spatial and temporal structure of the fast waveguide mode in order to predict the behavior of the resulting FLRs.

Further of interest is how the waveguide responds to different forms of magnetopause driving: symmetric or asymmetric about noon; localized flank driving. Previous work where the waveguide was driven with a broadband stimulus showed that the waveguide will respond with normal modes whose natural frequencies lie within the frequency spectrum of the driver (Elsden & Wright, 2018). However, the particular normal mode which is excited, and the efficiency of such fast mode resonance, will depend upon the structure of the driver. For example, a driver that is antisymmetric about noon will not excite waveguide modes that are symmetric about noon. This will then impact the FLRs driven. Such analysis of different magnetopause driving is further useful to understand how ULF waves may be driven by transient ion foreshock phenomena (M. D.; Hartinger et al., 2013; Shen et al., 2018; Wang et al., 2018), or other localized drivers such as magnetosheath jets (Plaschke et al., 2017).

This paper comprises the following sections: Section 2 summarizes the numerical model used for all of the simulations presented; section 3 considers how changing the equilibrium density profile affects FLR excitation; sections 4 and 5 deal with the effect of different magnetopause driving, considering an antisymmetric disturbance about noon and changing magnetic local time, respectively; section 6 is concerned with the theory behind the fast waveguide mode structure, which underpins the results in each of the previous sections; concluding remarks are presented in section 7.

2. Model

The model used in this paper is described in detail by Wright and Elsden (2016) and Elsden and Wright (2017), with a summary also given in section 2 of Elsden and Wright (2018). For the reader's convenience, a few of the key features will be restated here along with a reference schematic of the coordinates used shown in Figure 1.

We employ a field-aligned orthogonal coordinate system, adapted from a classical 2-D dipole for improved numerical efficiency. The coordinates (α, β, γ) represent the "radial," "azimuthal," and field-aligned directions, respectively, as pictured in Figure 1a. The linearized ideal MHD equations for a cold plasma are formulated in these coordinates (equations (9)–(13); Elsden & Wright, 2017), and solved numerically using a second-order leapfrog trapezoidal finite difference scheme (Zalesak, 1979; the application of this scheme is well presented by Rickard & Wright, 1994, equations (12)–(15)). The time step used to advance the

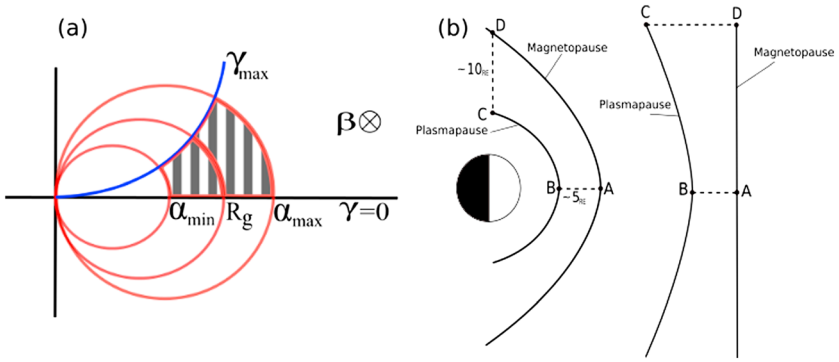

Figure 1. (a) Coordinate system used in the simulations (not to scale). Gray shaded region is the simulation domain. Red lines (constant α) are magnetic field lines, with the blue line (constant γ) being the upper boundary of the simulation. (b) Schematic of the real magnetosphere in the equatorial plane (left) and our model waveguide (right) demonstrating key boundaries and distances, along with the flaring nature of the waveguide on the flanks.

system is chosen to maintain a Courant number of $C \leq 0.4$, which is selected for numerical stability while not reducing the time step too restrictively. The stability and accuracy of the method under these conditions is evidenced by the conservation of energy, typically to one part in 10^4 at the end of a simulation. All quantities presented in this paper are dimensionless, given that the equations being solved (see Elsden & Wright, 2017, equations (9)–(13)) have been normalized by characteristic values: lengths by R_0; magnetic field by the background field $B_0 = B(\alpha_{max} = R_0, \beta = 0, \gamma = 0)$; densities by $\rho_0 = \rho(\alpha_{max} = R_0, \beta = 0, \gamma = 0)$; velocities by $V_0 = B_0\sqrt{\mu_0\rho_0}$; times by $t_0 = R_0 V_0$.

The following boundary conditions are applied: the radial inner boundary (α_{min}) is perfectly reflecting, while the outer radial boundary (α_{max}) is driven with a magnetic pressure perturbation (proportional to the field-aligned magnetic field perturbation), to be later specified in each individual case. The azimuthal boundaries (β_{min}, β_{max}) act as an open-ended waveguide through the use of dissipative buffer zones, which sufficiently damp any perturbations such that they cannot return to the solution region of interest. These were tuned so that waves incident upon the dissipative region suffered less than 5% reflection. In the equatorial plane ($\gamma = 0$), a symmetry condition is used such that the full solution represents a fundamental mode over the field line length. At the ionospheric end of the field line (γ_{max}), the velocity has a node resulting in a perfectly reflecting condition. The value of specific parameters used in each of the simulations will be stated in the corresponding section.

3. Changing the Alfvén Speed Gradient

Resonant coupling persists in 3-D, even in highly nonaxisymmetric equilibria (Elsden & Wright, 2018). In this section, we investigate the effect of steepening the Alfvén speed gradient in the azimuthal (β) direction on the efficiency of resonant coupling. Figure 2 displays the results from three simulations, where only the equilibrium Alfvén speed profile is changed (the pressure imposed on the magnetopause is unchanged). The simulations have the following basic parameter settings: α: 0.3 → 1.0; β: −2.25 → 2.25; γ: 0→ 0.455; grid size (351, 451, 51). The outer boundary at $\alpha = 1.0$ is driven with a perturbation symmetric about the noon meridian ($\beta = 0$) of the form $b_\gamma(\beta, \gamma, t) = \cos^2(k_\beta\beta)\cos(k_\gamma\gamma)\sin^2(t/\tau_d)$ over $-1 \leq \beta \leq 1$ (as indicated by the thick black lines on the right-hand edge of each panel), where $k_\beta = \pi/2$, $k_\gamma = 2\pi/\lambda_\gamma = 3.4523$, and $\tau_d = 0.625$. The magnetopause boundary is driven over t: 0→ 1.9635, after which b_γ is set to 0 on the outer boundary for the rest of the simulation. This results in a broadband stimulus, which will excite natural waveguide modes within the frequency bandwidth of the driver (Elsden & Wright, 2018). It is these fast modes which then drive the FLRs in these simulations. The structure of the driver (and others used later in the paper) is idealized to cleanly excite particular waveguide modes of the system. To model the solar wind realistically, more complex forms of driving should be used, though that is beyond the scope of this work.

Figure 2 plots the square root of the kinetic energy in the equatorial plane at time $t = 14.094$, which we can use as an indicator of FLRs (Elsden & Wright, 2018). In the left-hand panel of Figure 2, the Alfvén speed is uniform; that is, $V_A = 1$ everywhere. In the middle panel, V_A varies gently with azimuth, decreasing from $V_A = 1$ at noon to $V_A = 0.6$ on the flanks. In the right-hand panel, V_A varies steeply with azimuth over $-1 \leq$

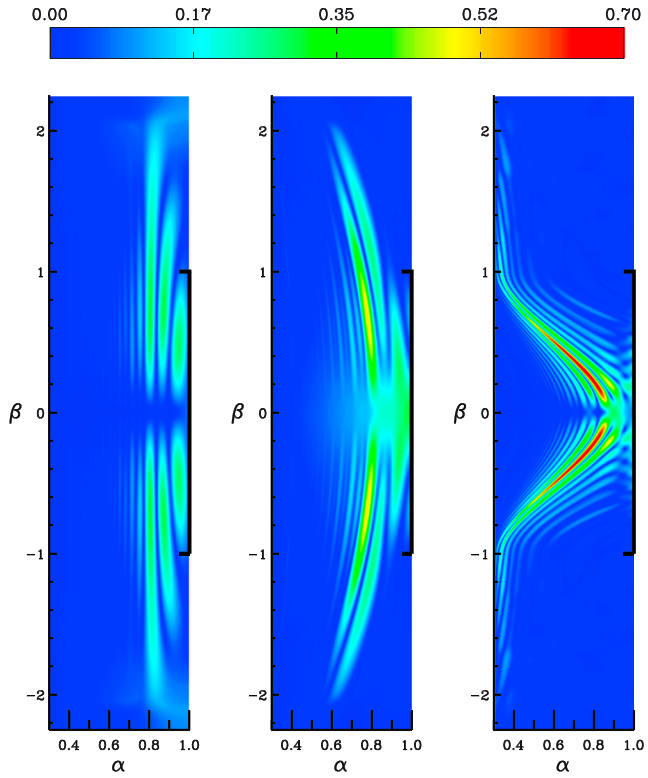

Figure 2. Square root of the kinetic energy in the equatorial plane for: (left) Uniform V_A; (middle) gently varying $V_A(\beta)$; (right) sharply varying $V_A(\beta)$. All use a symmetric driver about noon ($\beta = 0$) where the extent is indicated by the solid black lines on the right-hand edges.

$\beta \leq 1$, before becoming uniform ($V_A = 0.2$) for $|\beta| > 1$. There are many interesting features developed by these simplified simulations. First, the results indicate the smooth progression of the FLR features as the medium moves from 2-D (left) to 3-D (middle and right). This reenforces that 3-D resonant coupling is a robust feature and does not require special circumstances to occur. Indeed, the 3-D nonuniformity can enhance the resonant coupling, as indicated in Figure 2 by the increased amplitude of the resonance in the right-hand panel. The nonuniformity of the medium can generate enhanced gradients in the magnetic pressure, which are critical for resonant coupling (Elsden & Wright, 2017).

The extent of the ridges in the kinetic energy (normal to the main ridge) apparent in each of the panels of Figure 2 is controlled by the frequency bandwidth of the driver. Since the driver is broadband, there is a broad spatial resonance excitation, which reveals the structure generated through phase mixing, due to each field line responding at its own natural frequency. The dominant fast mode frequency can be determined from the peak in a fast Fourier transform of b_γ (indicative of the fast mode). Hence, given the equilibrium and the driving frequency peak and bandwidth, the spatial region in which the FLR will be excited can be accurately predicted by using the Resonance Map, as demonstrated in Figure 8 of Elsden and Wright (2018).

4. Effect of Driver Symmetry

In this section, we explore how the resulting FLR wave fields differ for an antisymmetric driver about noon (the simulations presented in Figure 2 used a symmetric driver). Figure 3 plots the square root of the kinetic energy in the equatorial plane for a magnetopause driver of the form

$$b_\gamma(\beta,\gamma,t) = \begin{cases} \sin^2\left(k_\beta\beta\right)\cos(k_\gamma\gamma)\sin^2(t/\tau_d), & -1 \leq \beta < -0.5 \\ -\sin(k_\beta\beta)\cos(k_\gamma\gamma)\sin^2(t/\tau_d), & -0.5 \leq \beta < 0.5 \\ -\sin^2\left(k_\beta\beta\right)\cos(k_\gamma\gamma)\sin^2(t/\tau_d), & 0.5 \leq \beta < 1.0 \end{cases} \quad (1)$$

with $k_\beta = \pi$, which acts over $0 < t < \pi\tau_d$. The other parameters are unchanged from previous simulations and the same Alfvén speed profile is used as in the middle panel of Figure 2. The reason for concentrating

on this case is that the degree of waveguide flaring on the flanks is most similar to that in the Earth's magnetosphere. The resulting FLR structure is markedly different from the symmetric case. The azimuthal nodal structure has changed, with the peak amplitude now situated at noon ($\beta = 0$), with approximate nodes in the kinetic energy around $\beta = \pm 0.5$. These are correlated with the azimuthal gradients in the magnetic pressure ($\sim \partial b_\gamma / \partial \beta$) present in the excited waveguide mode which has been driven by the antisymmetric driving about noon. At noon, based on the $\sin(k_\beta \beta)$ dependence over $-1 \leq \beta \leq 1$, the gradients are largest and hence the larger amplitude response is observed. At $\beta = \pm 0.5$, $\partial b_\gamma / \partial \beta = 0$ (as indicated by the red tick marks on the right-hand plot axes), which causes the FLR fields to have approximate nodes there.

The resonance is driven by the excited waveguide mode. However, the structure of the initial driver is important in determining which waveguide modes are excited. Thus, it is imperative to understand both the nature of the driver and the waveguide modes supported by the medium in order to predict the strength and location of the resonant coupling. These points will be treated in more detail in section 6.

5. Changing the Driver Location

The previous section showed the dramatic change to the FLR structure caused by having a symmetric/antisymmetric driver. A general magnetopause driver may be decomposed into components that have an odd or even symmetry about noon, so it is expected that driving the magnetopause "off center" will excite both odd and even waveguide modes, along with their associated FLRs. Figure 4 displays the square root of the kinetic energy in the equatorial plane for three simulations with the driver centered on (left) $\beta = 0$; (middle) $\beta = 0.5$; and (right) $\beta = 1.0$. In these cases, the driver has a similar form to that used in Figure 2, namely, $b_\gamma(\beta, \gamma, t) = \cos^2(k_\beta(\beta - \beta_c))\cos(k_\gamma \gamma)\sin^2(t/\tau_d)$, $k_\beta = \pi/2$ and β_c is changed to shift the driver to positive β as required. In each case, the driver has an azimuthal extent of 2; that is, left panel of Figure 4 is driven over $-1 \leq \beta \leq 1$, middle panel over $-0.5 \leq \beta \leq 1.5$, and right panel over $0.0 \leq \beta \leq 2.0$, as indicated by the thick black lines at the right edge of each panel.

Figure 4 shows a clear progression: As the driver moves duskward (larger β) the FLRs drift duskward too. (This is qualitatively the same as seen in Figure 2 of Degeling et al., 2010.) It is interesting to note that the largest FLR response is approximately located on the shoulders of the driver profile in β, that is, $\beta \approx -0.5, 0.5$ (left panel), $\beta \approx 0.0, 1.0$ (middle panel), and $\beta \approx 0.5, 1.5$ (right panel, shown with red tick marks). This corresponds to where the azimuthal magnetic pressure gradient of the driver profile is largest and so can drive a large FLR response. However, the nodal/antinodal structure of the FLRs is not so easy to interpret for a driver with an arbitrary location. Our model equilibrium is symmetric about noon, so the fast modes it supports are exactly symmetric or antisymmetric about noon. These modes are a property of the equilibrium. The left-hand panel of Figure 4 has a driver that is symmetric about noon, and so will excite waveguide modes that are symmetric also. (The amplitude of antisymmetric waveguide modes in this case are identically zero.) All the symmetric waveguide modes have an antinode of magnetic pressure at noon, and hence a node of the azimuthal magnetic pressure gradient here, which explains the clear node of FLRs seen at noon.

When the driver is not centered on noon (middle and right panels of Figure 4) the nodal structure of the FLRs is not very clear. This can be appreciated by realizing that the driver in these cases will excite both symmetric and antisymmetric waveguide modes. In particular, the antisymmetric waveguide modes have a node of magnetic pressure at noon, and hence an antinode of the azimuthal magnetic pressure gradient. Therefore, antisymmetric waveguide modes will drive FLRs at noon, in contrast to the symmetric modes in the left-hand panel. This reasoning explains the lack of an FLR node at noon in the middle and right panels, and also the lack of a clear nodal structure in general. It should also be noted that changing the spatial profile of the driver will affect the amplitude of the waveguide modes that are excited. In principle, if these amplitudes were determined, the Alfvén wavefields established by each waveguide mode could be determined and then summed appropriately to construct Figure 4. This demonstrates how knowledge of the fast waveguide modes is crucial for an interpretation of the FLR response.

Figure 5 presents time series and fast Fourier transforms of b_γ from two locations in the waveguide in each of the three simulations shown in Figure 4. The black lines are from the simulation with the driver centered on $\beta = 0.0$ (noon, left panel of Figure 4), the red lines are for the driver centered on $\beta = 0.5$ (middle panel of Figure 4), and the blue lines are for the driver centered on $\beta = 1.0$ (right panel of Figure 4). The top panels are taken from the location ($\alpha = 0.85$, $\beta = 0.0$), that is, noon and close to the magnetopause, while

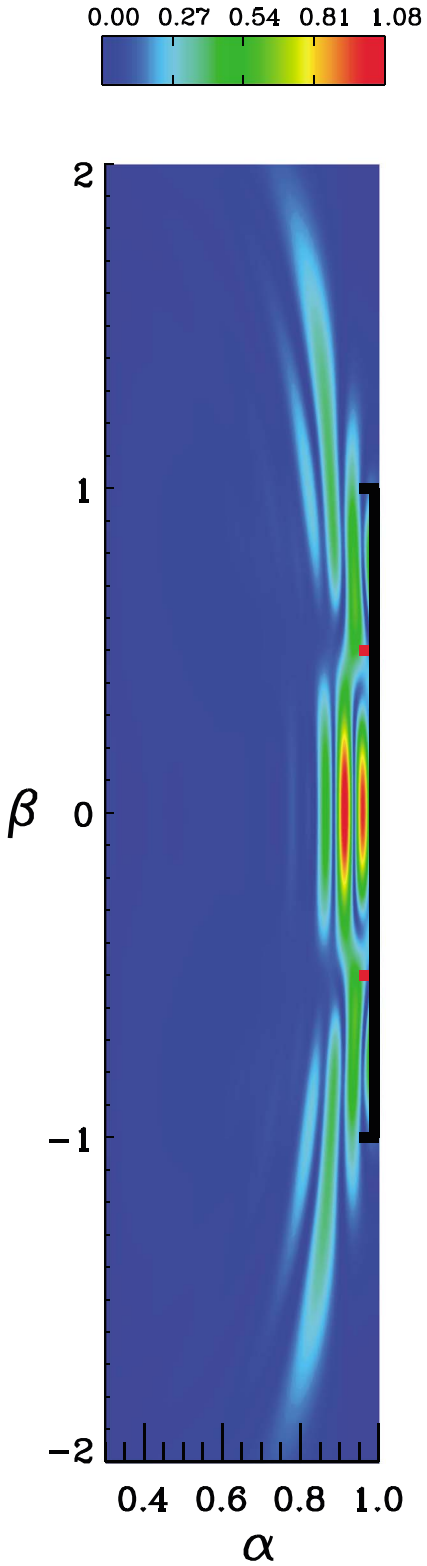

Figure 3. Square root of the kinetic energy in the equatorial plane, for an asymmetric driver about noon ($\beta = 0$). The solid black line on the right-hand side indicates the azimuthal extent of the driver, with the red tick marks denoting where the azimuthal magnetic pressure gradient of the driver is 0.

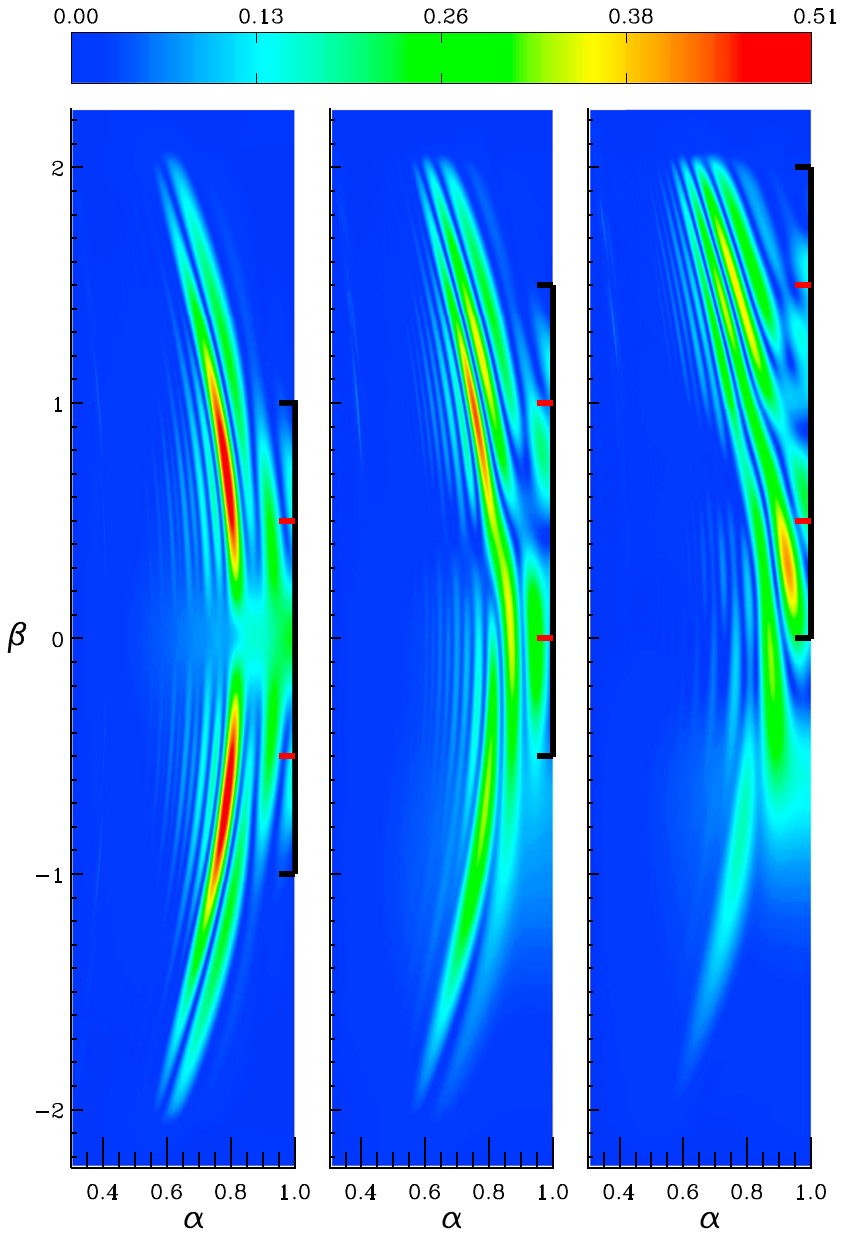

Figure 4. Square root of the kinetic energy in the equatorial plane for a driver centered on (left) $\beta = 0$; (middle) $\beta = 0.5$; and (right) $\beta = 1.0$. The solid black lines on the right edges of each panel indicate the azimuthal extent of the driver, with the red tick marks demarcating the azimuthal half-width of the driver profile.

the bottom panels are from ($\alpha = 0.54$, $\beta = 0.58$), which is further downtail. The stand out feature is that in all of the simulations and at each location, the frequency is the same (see right panels). To restate this, regardless of where the waveguide is driven or the location of the satellite measurement, the frequency is the same. This introduces the idea that when a normal mode of the waveguide is excited, it has a well-defined frequency, which is the same at all locations, which is perhaps surprising given the inhomogeneity present in the simulations. Indeed, this explains the similar locations of the resonant shells in each panel of Figure 4.

The amplitudes of the time series also reveal an important feature. The initially large amplitude of the black line in the top left panel, and the red line in the bottom left, can be accounted for by the time series being sampled close to where the driver has a maximum. However, whether at noon (top left) or afternoon (bottom left), the black line persists at later times with a larger amplitude than the red or blue. This can be explained by considering ray trajectories of the fast modes launched by each of the different drivers, shown in Figure 6.

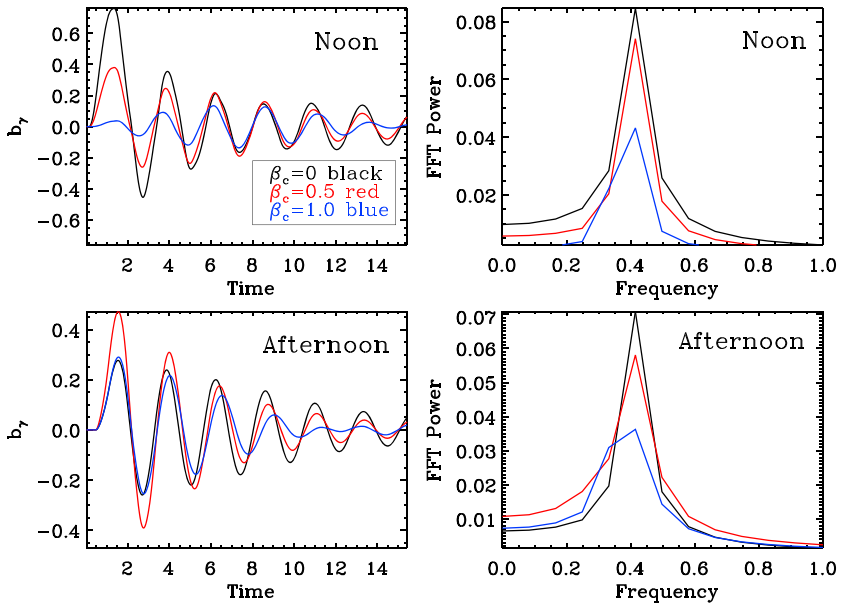

Figure 5. Time series (left) and fast Fourier transforms (right) of b_y taken from (top) ($\alpha = 0.85$, $\beta = 0.0$) at noon; (bottom) ($\alpha = 0.54$, $\beta = 0.58$) in the afternoon sector, for the three simulations (black: left; red: middle; and blue: right) in Figure 4, as indicated by the legend in the top left panel, where β_c is the center of the driving profile.

The left hand panel demonstrates how rays refract due to the decreasing of the Alfvén speed away from noon. When driven symmetrically around noon, fast mode rays can remain here (bouncing back and forth along the noon meridian) for a significant period before eventually propagating tailward, and so should be the slowest decaying mode. This corresponds to a longer-lived waveguide mode and a longer-driven resonance (Wright, 1994), which explains the persisting larger amplitude of the black line in the time series in Figure 5. For flank driving (as in the middle panel of Figure 6), the rays experience an azimuthal variation in V_A (unlike those at noon) so refract and start to propagate azimuthally from the outset. These rays correspond to modes that will decay more quickly than those associated with noon driving. Consequently, these waves do not drive as significant a resonant response as those at noon. The red lines indicate a wave which has initially propagated toward noon, but due to refraction ends up propagating toward dusk, as also seen in

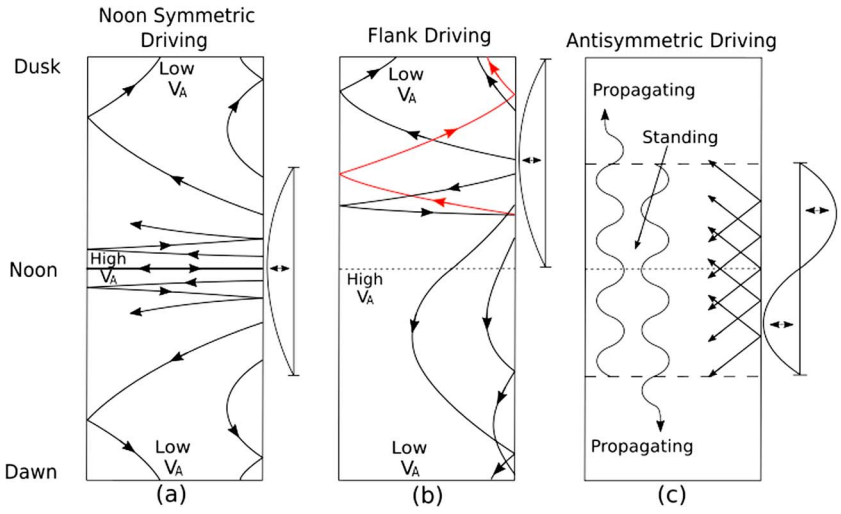

Figure 6. Sketches of ray trajectories highlighting the refraction in a waveguide (which is symmetric about noon) due to gradients in the Alfvén speed for (a) noon symmetric driving; (b) flank driving. The red lines in panel (b) represent a ray which has changed direction in azimuth. Panel (c) depicts wave vectors and resulting wave modes from an antisymmetric push about noon, launching more inclined waves which propagate tailward more quickly.

simulations by Wright et al. (2018). The right-hand panel deals with an antisymmetrically driven waveguide and will be discussed further in the following section.

6. Fast Mode Nodal Structure

To properly interpret the previous results, a full understanding of the fast waveguide normal mode structure is required. Consider a normal mode of the following form:

$$b_{\gamma m}(\alpha, \beta, \gamma, t) = f(\alpha, \beta, \gamma)e^{i\omega t}, \tag{2}$$

where the function f represents the complex spatial dependence of the mode, which oscillates in time with frequency ω. The variable $b_{\gamma m}$ represents the full complex mode for the magnetic pressure perturbation, the real part of which corresponds to the physical compressional field perturbation that would be measured by a satellite or solved for in a simulation (this is just the b_γ of previous sections). For a leaky mode, as in the case of our simulations where energy can propagate out of the waveguide, the frequency ω will be complex with form $\omega = \omega_r + i\omega_i$. Hence, equation (2) can be written as

$$b_{\gamma m}(\alpha, \beta, \gamma, t) = f(\alpha, \beta, \gamma)e^{i\omega_r t}e^{-\omega_i t}. \tag{3}$$

The real and imaginary parts of the function f will give all the information required to construct the full complex spatial solution. This is a critical component to understanding the FLRs which such waveguide modes excite.

To study the normal waveguide modes in detail, we tailor our simulations accordingly, which have the following basic properties: α: $0.3 \rightarrow 1.0$; β: $-3 \rightarrow 3$; γ: $0 \rightarrow 0.455$; grid size $(301, 601, 41)$. The Alfvén speed varies smoothly with azimuth (β), similar to the profile used in the simulations shown in Figure 4. To isolate the different natural waveguide harmonics, we first drive the system with a broadband perturbation and observe the dominant frequencies which appear. These will correspond to the natural frequencies of the leaky waveguide modes. We can then drive at one of these frequencies for several cycles to establish the mode fully (as it will respond resonantly and grow secularly in time), before stopping driving and letting the system oscillate freely and decay. This undriven decay phase can be used to construct the complex spatial structure of the normal mode. For reference, the driver has the form $b_\gamma(\beta, \gamma, t) = \cos^2(k_\beta\beta)\cos(k_\gamma\gamma)\sin(t/\tau_d)$ over $-1 < \beta < 1$ (and is zero elsewhere) for the symmetric runs, with $k_\beta = \pi$. For the antisymmetric runs a similar profile to that described by equation (1) is used, with $k_\beta = \pi/2$ and a $\sin(t/\tau_d)$ time dependence, where τ_d and the driving duration will be later listed for each simulation presented.

Figure 7 displays various analyses of two simulations, the first being symmetrically driven, the second antisymmetrically driven, where the fundamental radial waveguide mode is excited. (Both simulations use $\tau_d = 0.303$, driven for a duration $t = 12.381$). Figures 7g and 7h show the establishing of the normal mode in the symmetric and antisymmetric cases, by plotting b_γ as a function of time at $(\alpha, \beta, \gamma) = (0.8, 0.0, 0.0)$ and $(0.8, 0.51, 0.0)$ respectively. The initial growth phase during driving ($0 < t < 12.381$) is followed by decay of the free oscillation. Figures 7a–7d plot color contours of b_γ (indicative of the fast mode) in the equatorial plane for the symmetric (a and b) and antisymmetric (c and d) runs, taken at times (a) $t_0 = 13.84$, (b) $t = 14.32$, (c) $t = 14.55$, and (d) $t = 15.03$. To understand what plotting b_γ from the simulation represents, consider taking the real part of the right-hand side of equation (3), evaluated in the equatorial plane at $\gamma = 0$, which yields

$$\begin{aligned} b_\gamma = Re\left[b_{\gamma m}\right] &= Re\left[f(\alpha, \beta)e^{i\omega_r t}e^{-\omega_i t}\right] \\ &= \cos(\omega_r t)f_r(\alpha, \beta)e^{-\omega_i t} - \sin(\omega_r t)f_i(\alpha, \beta)e^{-\omega_i t}, \end{aligned} \tag{4}$$

where f_r and f_i are the real and imaginary parts of f. Equation (4) shows that at times $t = 2n\pi/\omega_r$ for $n = 0, 1, 2...$, $b_\gamma = f_r$ (neglecting the exponential decay term). Equally at times $t = (4n + 1)\pi/2\omega_r$ for $n = 0, 1, 2...$, $b_\gamma = -f_i$, again neglecting the exponential decay term. These times can be identified in the simulation through the temporal variation of b_γ (e.g., panels g and h). The times selected in Figures 7a and 7c are such times where b_γ corresponds to the real part of f, namely, f_r, while (b) and (d) are taken one quarter of a cycle later, and hence determine the imaginary part, f_i. In panel (a), the symmetric structure of the driver about noon ($\beta = 0$) has set up a symmetric normal mode within the waveguide, with a clear antinode of b_γ at noon. A quarter of a cycle later, the signal has propagated tailward resulting in the two

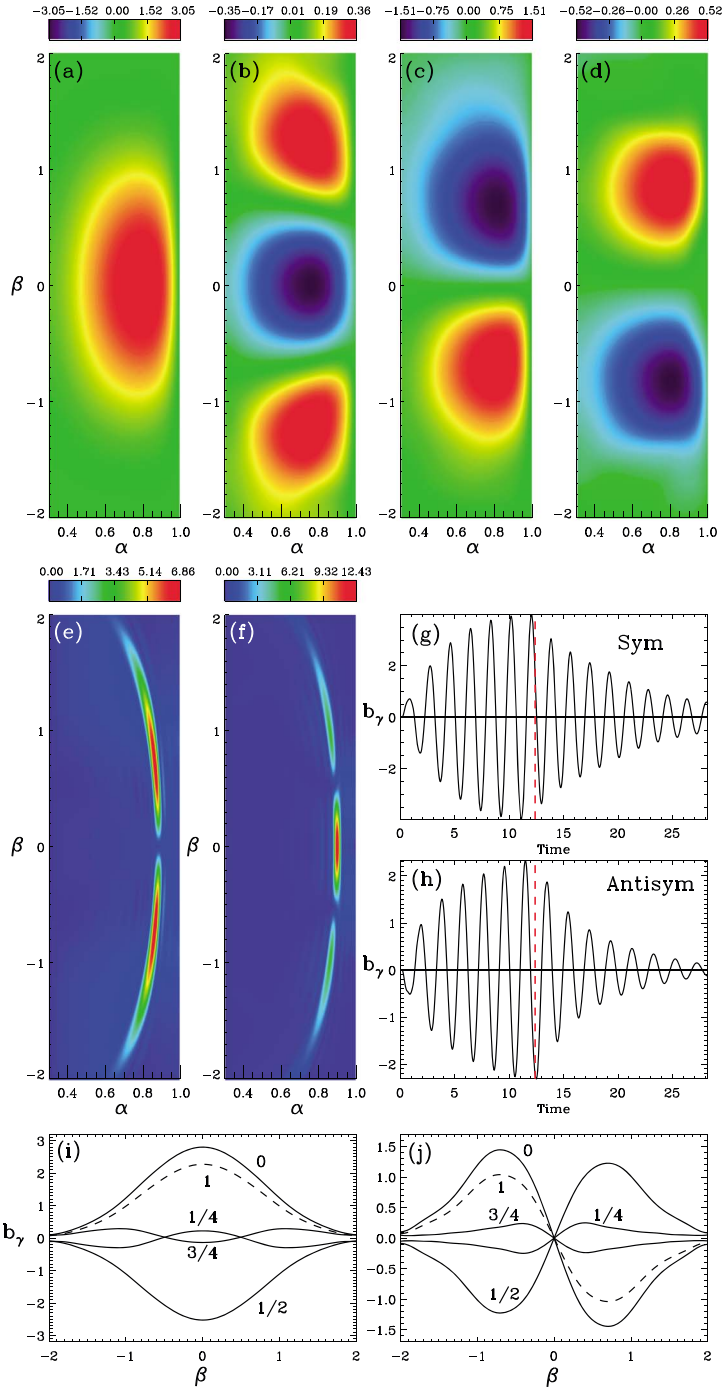

Figure 7. Simulations to highlight waveguide normal mode structure. (a) Color contour of b_γ in the equatorial plane at $t = 13.84$ and (b) $t = 14.32$, for a symmetric driver about noon, exciting the fundamental radial and field-aligned harmonic. (c) Color contour of b_γ in the equatorial plane at $t = 14.55$ and (d) $t = 15.03$, for an antisymmetric driver. (e) Symmetric driver, square root of the kinetic energy in the equatorial plane. (f) Same as (e) but for antisymmetric driver. (g) The b_γ time series from point (0.8,0.0,0.0), symmetric case. (h) The b_γ time series from point (0.8,0.51,0.0), antisymmetric case. (i) Normal mode reconstruction of $b_\gamma(\beta) = Re(b_{\gamma m})$ at $\alpha = 0.872$ in the equatorial plane ($\gamma = 0$) over one cycle. Each line is taken a quarter of a cycle apart as labeled, with the dashed line labeled '1' being a full cycle later than the solid line labeled '0'. (j) Same as (i) for antisymmetric case, taken from $\alpha = 0.895$.

peaks at larger $|\beta|$ in panel (b). In the antisymmetric case, there is a clear node of b_γ at noon in panel (c) which persists over a quarter of a cycle (panel d).

Now that the real and imaginary parts of f have been identified via the simulation, they can be used in equation (4) to reconstruct the full normal mode solution for b_γ. Figures 7i and 7j show a cut through this normal mode reconstruction for b_γ as a function of β over one cycle for the symmetric and antisymmetric cases, respectively. The fixed α location in each case is chosen to pass through the center of the FLR maxima as shown in panels (e) and (f) ($\alpha = 0.872$ for the symmetric, $\alpha = 0.895$ for the antisymmetric), and the cuts are taken in the equatorial plane ($\gamma = 0$). The start times in each case (as used in panels a and c) are labeled with a "0" in panels (i) and (j). The other cuts are plotted at intervals of a quarter of a cycle as labeled, with the final cut drawn as the dashed line, one cycle after the initial time. Further included is the decay of the form $e^{-\omega_i t}$, where ω_i is measured using the decay evident in panels (g) and (h) ($\omega_i = -0.1109$ for symmetric, $\omega_i = -0.1676$ for antisymmetric). This is clear in panels (i) and (j) by the decreased amplitude of the dashed lines (1) compared to the initial state (0) one cycle earlier. The key point about these plots is that they elucidate the spatial structure of the normal mode, and hence we can understand where the appropriate gradients will form necessary to efficiently drive Alfvén resonances.

This is well demonstrated by Figures 7e and 7f, which display the square root of the kinetic energy in the equatorial plane at a late simulation time ($t = 13.84$) for the symmetric and antisymmetric cases, respectively. The resonant response can be clearly matched up with the presence of azimuthal gradients in Figures 7i and 7j. The symmetric case has an extremely well-defined node in the resonant fields at noon, matching where $\partial b_\gamma/\partial\beta = 0$ in Figure 7i. Further, the largest gradients occur at $\beta \simeq \pm 0.8$ from panel (i), which agrees with the FLR maximum in panel (e). The antisymmetric case has a clear maximum in the kinetic energy at noon, consistent with the maximum gradient in b_γ in Figure 7j. The nodes of the azimuthal magnetic pressure gradient occur at $\beta \simeq \pm 0.7$ from panel (j), which matches very clearly with the FLR nodes in panel (f). It is interesting to note that despite the strong resonant response, there is no trace of the resonance structure in the color contour plots of b_γ in Figures 7a–7d, showing the incompressible nature of Alfvén waves.

Figure 8 displays results for the symmetric and antisymmetric driving of the third radial harmonic, for the same equilibrium as used in Figure 7. The waveguide is driven until $t = 3.617$, with a value of $\tau_d = 0.068$ (for the same driver profile used in Figure 7). For this case where the driving frequency is higher to excite the third harmonic, there is no significant Alfvén resonance within the waveguide. Thus, the decay of the fast mode is dominated by leakage into the tail (rather than resonant coupling), and permits a cleaner comparison of decay rates and the effect of symmetry/antisymmetry of the driver than the results in Figure 7. Figures 8a–8d display color contour plots of b_γ in the equatorial plane in the same fashion as Figures 7a–7d, associated with the real/imaginary parts of $f(\alpha, \beta, 0)$ for symmetric/antisymmetric driving (times given in the figure caption). The third radial harmonic structure is evident in the real parts (a and c) at $\beta = 0$, together with a shorter azimuthal wavelength at larger $|\beta|$ (see Movie S1 in the supporting information for the movie of the temporal development).

Panels (g) and (h) show cuts in β of b_γ (solid) and u_β (dashed) at $\alpha = 0.848$ for the symmetric (g) and antiymmetric (h) cases. There is a spatial phase difference of $\pi/2$ between these signals in the central region, consistent with a standing mode structure, while they are in/out of phase for $|\beta| > 1$, indicative of a propagating mode azimuthally. This neatly explains the nodal structure visible in panels (a)–(d) and can be clearly seen in Movie S1 (available in the supporting information). Panels (e) and (f) show time series of b_γ from points (0.848,0.0,0.0) and (0.848,0.51,0.0) in the symmetric and antisymmetric runs, respectively. Comparing these two figures, it is clear that the antisymmetric mode decays far more rapidly, which would greatly affect the driving of an Alfvén resonance. Such bias is also evident, albeit to a lesser degree, in Figures 7g and 7h.

To explain this, consider the right-hand panel of Figure 6, demonstrating the waves launched by an antisymmetrically driven magnetopause about noon. The form of the driver is given schematically to the right-hand edge of the plot. Importantly, the driver has a standing nature in azimuth (β). This will excite waveguide modes that have a standing nature locally, which can be decomposed into a superposition of waves propagating dawnward and duskward. Effectively, such a driver will launch waves at an oblique angle to both positive and negative β (dusk/dawn). In the central region, the summation of these oppositely propagating waves will form a standing mode structure. Further downtail, however, (outside of the driving region where

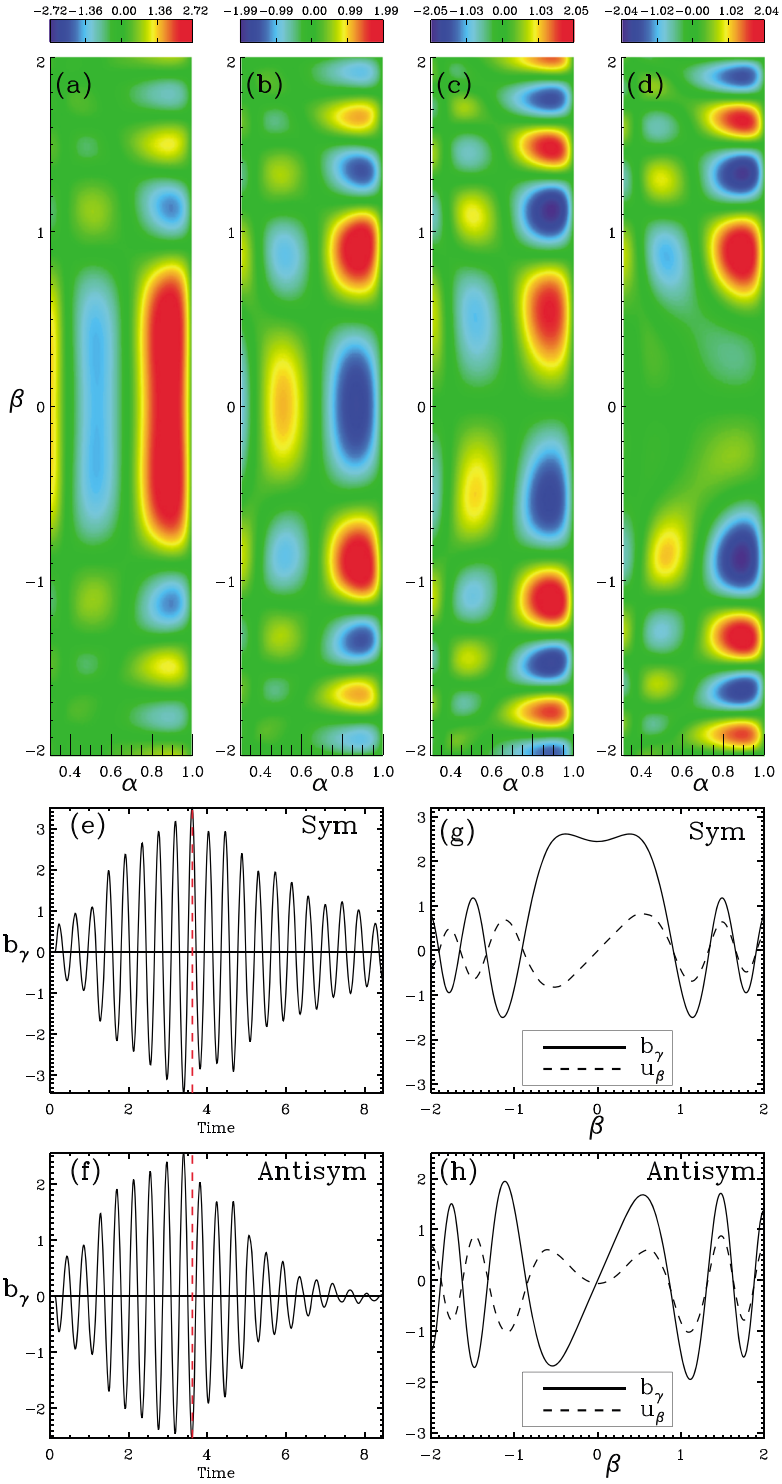

Figure 8. Symmetric and antisymmetric driving exciting the third radial harmonic. Color contour plot of b_γ in the equatorial plane at (a)$t = 4.07$ and (b) $t = 4.18$ a symmetric driver about noon. Color contour plot of b_γ in the equatorial plane at (c) $t = 4.22$ and (d) $t = 4.33$ for an antisymmetric driver. (e) The b_γ time series from point (0.848,0.0,0.0), symmetric case. Red dashed line represents the time where the driver is switched off. (f) The b_γ time series from point (0.848,0.51,0.0), antisymmetric case. (g) The $b_\gamma(\beta)$ (solid) and $u_\beta(\beta)$ (dashed) at $\alpha = 0.848$, $\gamma = 0$, $t = 4.07$, symmetric case. (h) Same as (g) but for $t = 4.22$, antisymmetric case.

there will exist oppositely propagating waves of significant amplitude) the modes will be purely propagating tailward. This effect will also be aided by refraction as previously mentioned in the discussion of the left and middle panel of Figure 6. Thus, the rays launched from an antisymmetric driver always have some azimuthal propagation and can never follow the path of the long-lived rays confined to the noon meridian, shown in the left-hand panel of Figure 6.

The waveguide modes shown in Figures 8a–8d are third harmonic in α and fundamental in γ. Their harmonic number in β is not so obvious: they are actually first harmonic in β (panels a and b) and second harmonic in β (c and d), although the many nodes in β may make this statement surprising. To help justify our claim we have included an appendix which provides analytical solutions for a simplified waveguide that is nonuniform in β. In waveguides where the azimuthal variation of V_A has a minimum at noon, it is easy to see how refraction will partially trap waves here. When V_A has a maximum at noon, this process cannot operate, so how can we produce partially trapped modes at noon? In the appendix we show how the azimuthal variation in V_A causes partial reflection of azimuthally propagating waves, and it is this reflection that allows the partial trapping of waveguide modes at noon.

7. Concluding Remarks

This paper has considered the effects of various forms of magnetopause driving on the excitation of waveguide normal modes and, further, the impact of the waveguide mode structure on 3-D FLR excitation. Such effects of magnetopause driving on the waveguide modes of the magnetospheric system have, to our knowledge, not been studied before in such depth. The key results can be listed as follows:

1. The equilibrium determines the normal modes and where FLRs may form.
2. The driver determines the particular normal modes which are excited, and hence specifies exactly where FLRs will form given the frequency and spatial structure of the waveguide mode. Only through understanding the waveguide mode structure can the resulting FLRs be appropriately predicted.
3. Symmetric magnetopause disturbances about noon (for an equilibrium symmetric about noon) drive normal modes which can remain around to drive resonances for longer than antisymmetric magnetopause driving.
4. Magnetopause drivers that are antisymmetric about noon launch waves that propagate tailward more quickly than in the symmetric case. However, the steeper gradients generated in the fast mode can lead to more efficient coupling.

The aim of this study has been to illustrate the importance of understanding the structure of magnetospheric waveguide modes and their role in determining where FLRs are excited. We have done this using an idealized equilibrium in order to get clean, well-resolved simulation results. This has been achieved by employing a field-aligned coordinate system which has allowed for higher resolution than global MHD simulations. Future studies could include a more realistic magnetic field and density, informed by observations (e.g., Sandhu et al., 2017). These will affect the properties of the fast mode (e.g., Archer et al., 2017) and consequently the details of the FLRs they excite.

Appendix A: Eigenfrequencies and Normal Modes of a Cartesian Waveguide

In this appendix we investigate how a waveguide with an azimuthal variation in V_A can have eigenmodes that describe the partial trapping of fast mode energy at noon. To demonstrate the relevant properties, we examine a simple Cartesian waveguide in which x, y, and z correspond to "radial," "azimuthal" and field-aligned coordinates with noon at $y = 0$. The background magnetic field is uniform and aligned with the z direction. We assume the guide has reflecting boundaries at $x = 0$ and $x = L$ (where the normal displacement vanishes), and at $z = 0$ and $z = L$ (where the electric field vanishes). The waveguide is open ended ($-\infty < y < +\infty$). For simplicity we shall assume $V_A(y)$ to be independent of x and z and focus on modes with a fundamental standing structure in x and z, that is, $b_z \propto \cos(k_x x)\sin(k_z z)$, with $k_x = k_z = \pi/L$. We shall focus on the free oscillation of normal modes—that is, the behavior after the driving of the guide has stopped and take $b_{zm} \propto \exp(i\omega t)$ for such modes. Here b_{zm} represents the compressional magnetic field perturbation and is a complex quantity. It is the counterpart of $b_{\gamma m}$ in the main text, and the real part of b_{zm} corresponds to the physical perturbation that would be measured in an experiment or simulation.

Trapping is most commonly thought of as occurring where there is a minimum in V_A, in a similar way that a wave function in quantum mechanics can describe a trapped particle in a potential well. In this case wave refraction naturally turns rays away from regions of higher V_A and toward those where V_A is lower, potentially trapping energy around the minimum in V_A. A ray with a component of group velocity away from the minimum of V_A may be refracted and bent so that its motion is eventually reversed (at a turning point), and it starts moving back toward the minimum. Adopting the complementary picture of normal (or eigen-) modes, such a mode would have a sinusoidal spatial variation with azimuth on the low V_A side of the turning point and an exponentially decaying structure on the high V_A side. Such modes are completely trapped and have a real frequency. This picture is most likely to apply to the lowest-frequency modes. The behavior is slightly different for higher frequency modes as they can exceed the cut–off frequency and begin propagating in y on the high V_A side of the turning point and may allow transport of energy to $y = \pm\infty$. Such an undriven normal mode will be losing energy from the region around noon, so it will decay in time. Consequently, the frequency and k_y of such a mode will be complex, giving a variation in azimuth that is a mixture of exponential and sinusoidal.

For a realistic magnetosphere, V_A inside the magnetopause decreases on moving from noon to the flanks. This is the opposite situation to the familiar trapping picture described above. To appreciate how a realistic azimuthal V_A variation can produce partially trapped leaky modes we assume the following simplified $V_A(y)$,

$$V_A(y) = \begin{cases} V_1, & |y| < L \\ V_2, & |y| > L \end{cases} \tag{A1}$$

and assume $V1 > V2$ so refraction will not serve to trap rays around noon ($y = 0$).

The fast mode dispersion relation ($\omega^2 = V_A^2(k_x^2 + k_y^2 + k_z^2)$) can be used to determine the local wavenumber k_y which has different values for $|y| < L$ and $|y| > L$, denoted by

$$k_y = \begin{cases} k_{y1} = \sqrt{\omega^2/V_1^2 - k_x^2 - k_z^2}, & |y| < L \\ k_{y2} = \sqrt{\omega^2/V_2^2 - k_x^2 - k_z^2}, & |y| > L. \end{cases} \tag{A2}$$

In terms of the mode number in y, the odd modes (first, third, fifth, … harmonic) will have an antinode of b_z at $y = 0$, so may be taken to vary as

$$b_{zm} \propto \cos(k_{y1} y), \qquad |y| < L, \tag{A3}$$

whereas the even modes (second, fourth, sixth, … harmonic) will have a node of b_z at $y = 0$, so vary as

$$b_{zm} \propto \sin(k_{y1} y), \qquad |y| < L. \tag{A4}$$

In the regions $|y| > L$ the mode may propagate out of the guide, so has a form

$$b_{zm} \propto \exp i(\omega t - k_{y2} y), \qquad y > L, \tag{A5}$$

and a similar form for $y < L$ but with the minus sign replaced by a plus. The dispersion relation follows from imposing continuity of b_{zm} and $\partial b_{zm}/\partial y$ at $y = L$. The resulting dispersion relation for odd modes is

$$\cot\left(L\sqrt{\omega^2/V_1^2 - k_x^2 - k_z^2}\right) + i\frac{\sqrt{\omega^2/V_1^2 - k_x^2 - k_z^2}}{\sqrt{\omega^2/V_2^2 - k_x^2 - k_z^2}} = 0, \tag{A6}$$

while that for even modes is

$$\tan\left(L\sqrt{\omega^2/V_1^2 - k_x^2 - k_z^2}\right) - i\frac{\sqrt{\omega^2/V_1^2 - k_x^2 - k_z^2}}{\sqrt{\omega^2/V_2^2 - k_x^2 - k_z^2}} = 0. \tag{A7}$$

To demonstrate the partial trapping of modes, the mechanism responsible, and a clear justification of the mode number in y, we begin with a case having a large disparity in V_1 and V_2; specifically, we take

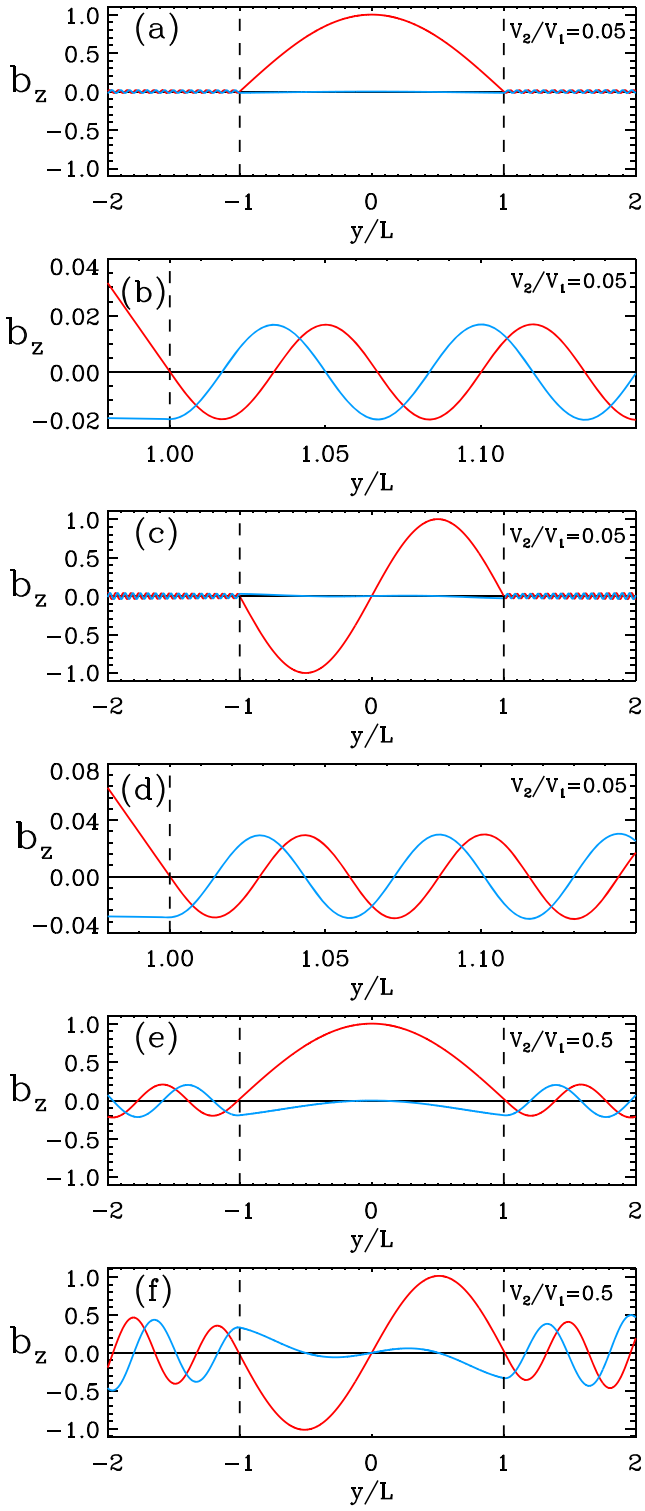

Figure A1. Real (red) and imaginary (blue) parts of b_z as a function of y (azimuth) for normal modes of a Cartesian waveguide with a step in the density at $y = 1$. (a) First harmonic for $V_2/V_1 = 0.05$, (b) close up of (a) around $y = 1$, where speeds change, (c) second harmonic for $V_2/V_1 = 0.05$, (d) close up of (c) around $y = 1$, (e) first harmonic for $V_2/V_1 = 0.5$, and (f) second harmonic for $V_2/V_1 = 0.5$. The dashed lines in each panel at $y = \pm 1$ demarcate the different speed regions ($V_A = V_1$ for $|y| < 1$ and $V_A = V_2$ for $|y| > 1$).

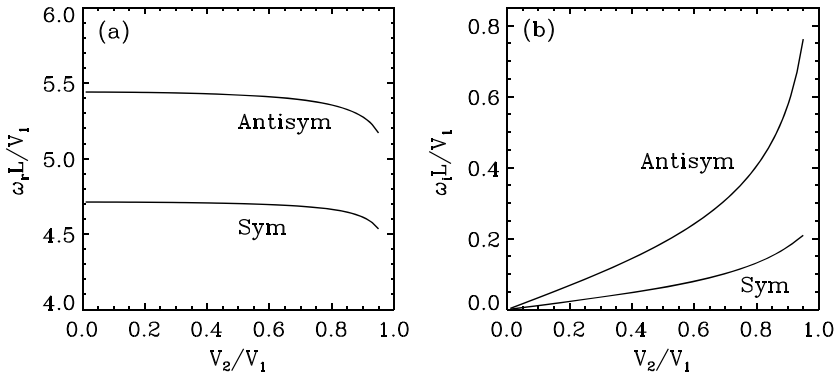

Figure A2. (a) Real frequency ω_r and (b) imaginary frequency ω_i as a function of the speed ratio V_2/V_1 for the first harmonic (symmetric) and second harmonic (antisymmetric) cases as labeled for the Cartesian waveguide.

$V_2 = 0.05V_1$. The lowest-frequency solution to the dispersion relations corresponds to the fundamental (first hamonic) and has a complex frequency of $\omega = \omega_r + i\omega_i = (4.71231 + i0.00556)V_1/L$ with $\omega_i \ll \omega_r$ indicating the mode decays very slowly over many cycles. This mode has a high degree of trapping, and a plot of the $b_{zm}(y)$ eigenfunction for $L = 1$ in Figure A1a reveals why.

The small V_2 in the region $|y| > 1$ is associated with a density 400 times that at $y = 0$ so represents an almost immovable plasma by comparison. This is why the amplitude of the mode for $|y| > 1$ is much less than that for $|y| < 1$. This can also be interpreted in terms of wave reflection at the interfaces at $y = \pm 1$. The (essentially standing) wave over $|y| < 1$ can be decomposed into left- and right-propagating waves. The wave propagating to the right is incident upon the jump in V_A at $y = 1$ and the classical transmission and reflection coefficients

$$T = \frac{2V_2}{V_1 + V_2}, \qquad R = \frac{V_2 - V_1}{V_1 + V_2} \tag{A8}$$

show that as $V_2/V_1 \to 0$ the amplitude of the transmitted wave tends to zero, and the incident wave is perfectly reflected. This results in the perfect trapping of a standing wave with nodes at $y = \pm 1$ and frequency $\omega L/V_1 = 3\pi/2 \equiv 4.71239 + i0$ (which is very close to that of the highly trapped mode in panel a). Evidently, the perfectly trapped mode may be termed the first harmonic on the basis of it being the lowest-frequency mode of the system and also its nodal structure. The highly trapped mode in Figure 1a is also the lowest-frequency mode of the $V_2/V_1 = 0.05$ system, and it is on this basis that we refer to it as the first harmonic. It actually has an infinite number of nodes as the eigenfunction extends to $y \to \pm\infty$, so the nodal classification is not helpful here. Indeed, a close up of the eigenfunction in the region $y > 1$ (Figure 1b) shows the real and imaginary components to be in quadrature, which is indicative of a propagating wave.

The second harmonic of the $V_2/V_1 = 0.05$ waveguide has a frequency $\omega = (5.44124 + i0.016685)V_1/L$ (close to the perfectly trapped $V_2/V_1 = 0$ case, which has $\omega L/V_1 = \sqrt{3}\pi = 5.441398 + i0$). The eigenmode for the second harmonic is shown in Figure 1c along with a close up of the mode structure in Figure 1d.

We now consider a waveguide with $V_2 = 0.5V_1$. The first harmonic is shown in Figure 1e and evidently has a larger amplitude where $|y| > 1$ compared to Figure 1a and is associated with an increased transmission coefficient. The frequency of this mode is $\omega = (4.70223 + i0.06250)V_1/L$, and the real part is still close to the perfectly trapped first eigenfrequency of $(4.71239 + i0)V_1/L$. However, when $V_2/V_1 = 0.5$, ω_i is around 10 times greater than when $V_2/V_1 = 0.05$, which is consistent with the transmission coefficient increasing by a similar amount. The $V_2/V_1 = 0.5$ second harmonic is shown in Figure 1f and has frequency $\omega = (5.42208 + i0.18824)V_1/L$, which shows a similar increase of ω_i to the $V_2/V_1 = 0.05$ case as is seen for the first harmonic.

The systematic increase of ω_i and gradual decrease of ω_r with increasing V_2/V_1 is shown in Figure A2. Note that the damping rate of the second harmonic (antisymmetric) is always much greater than the that of the first harmonic (symmetric), and may be understood in terms of the arguments given in section 6, discussing the behavior of symmetric and antisymmetric modes in Figure 6.

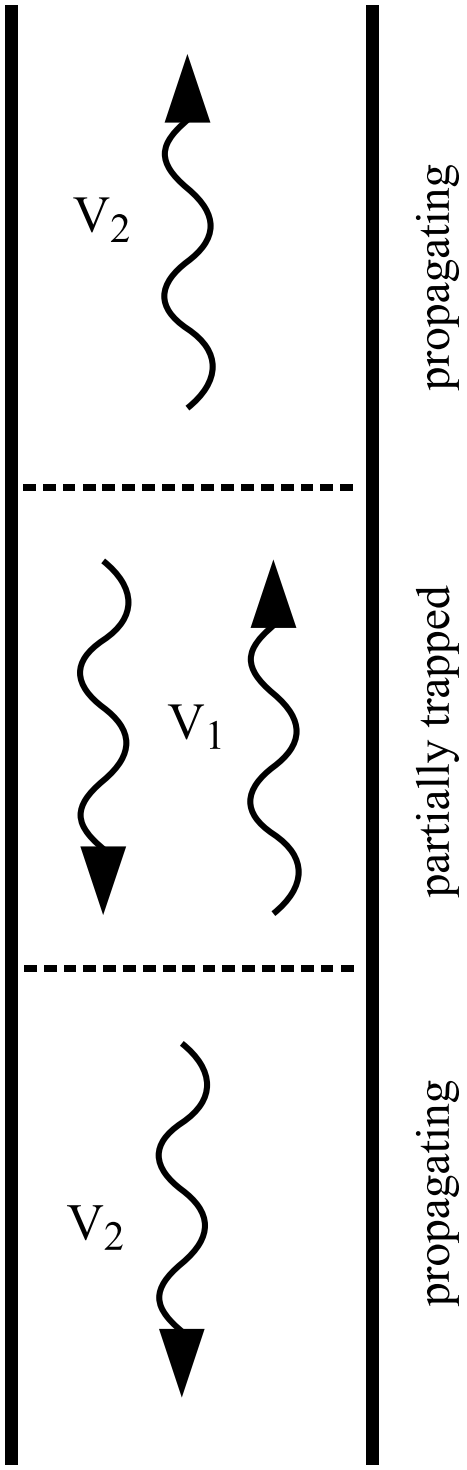

Figure A3. Schematic of a leaky waveguide. Along the length of the guide the Alfvén speed changes from V_2 to V_1 and back to V_2. (The medium supports standing waves across its width.) Fast waves can propagate along the length of the guide which extends to infinity. Energy is partially trapped in the V_1 section due to reflection and leaks off to infinity as the transmitted waves in the V_2 sections. The overall picture (in terms of a normal mode) is of an oscillating fast mode that decays in time.

Figure A3 shows a schematic of a leaky Cartesian waveguide. Waves initially in the V_1 trapped section will suffer some reflection at the V_1/V_2 boundary and so are partially trapped. The transmitted waves in the V_2 sections propagate off to infinity and drain energy from the central section. The behavior can also be viewed as a normal mode that has a mixed propagating/standing nature in the V_1 section and a solely propagating nature elsewhere. If the step in density is replaced by a distributed nonuniform V variation, there will still be partial reflection and transmission of waves associated with the nonuniformity, so leaky waveguide modes exhibiting temporal decay via a complex frequency are expected to be a robust feature of this type of system.

Acknowledgments
T. Elsden and A. N. Wright were funded by the Leverhulme Trust through research grant RPG-2016-071. A. N. Wright was also funded by STFC through consolidated grant ST/N000609/1. Data from simulation results are available on Figshare: https://figshare.com/authors/Tom_Elsden/4743264.

References

Allan, W., White, S. P., & Poulter, E. M. (1985). Magnetospheric coupling of hydromagnetic waves—Initial results. *Geophysical Research Letters*, *12*, 287–290. https://doi.org/10.1029/GL012i005p00287

Allan, W., White, S. P., & Poulter, E. M. (1986). Impulse-excited hydromagnetic cavity and field-line resonances in the magnetosphere. *Planetary Space Science*, *34*, 371–385. https://doi.org/10.1016/0032-0633(86)90144-3

Archer, M. O., Hartinger, M. D., Walsh, B. M., & Angelopoulos, V. (2017). Magnetospheric and solar wind dependences of coupled fast-mode resonances outside the plasmasphere. *Journal of Geophysical Research: Space Physics*, *122*, 212–226. https://doi.org/10.1002/2016JA023428

Chen, L., & Hasegawa, A. (1974). A theory of long-period magnetic pulsations: 1. Steady state excitation of field line resonance. *Journal of Geophysical Research*, *79*, 1024–1032. https://doi.org/10.1029/JA079i007p01024

Degeling, A. W., Rae, I. J., Watt, C. E. J., Shi, Q. Q., Rankin, R., & Zong, Q. G. (2018). Control of ULF wave accessibility to the inner magnetosphere by the convection of plasma density. *Journal of Geophysical Research: Space Physics*, *123*, 1086–1099. https://doi.org/10.1002/2017JA024874

Degeling, A. W., Rankin, R., Kabin, K., Rae, I. J., & Fenrich, F. R. (2010). Modeling ULF waves in a compressed dipole magnetic field. *Journal of Geophysical Research*, *115*, A10212. https://doi.org/10.1029/2010JA015410

Elsden, T., & Wright, A. N. (2017). The theoretical foundation of 3-D Alfvén resonances: Time-dependent solutions. *Journal of Geophysical Research: Space Physics*, *122*, 3247–3261. https://doi.org/10.1002/2016JA023811

Elsden, T., & Wright, A. N. (2018). The broadband excitation of 3-D Alfvén resonances in a MHD waveguide. *Journal of Geophysical Research: Space Physics*, *123*, 530–547. https://doi.org/10.1002/2017JA025018

Eriksson, P. T. I., Blomberg, L. G., Schaefer, S., & Glassmeier, K. H. (2006). On the excitation of ULF waves by solar wind pressure enhancements. *Annales Geophysicae*, *24*, 3161–3172. https://doi.org/10.5194/angeo-24-3161-2006

Harrold, B. G., & Samson, J. C. (1992). Standing ULF modes of the magnetosphere—A theory. *Geophysical Research Letters*, *19*, 1811–1814. https://doi.org/10.1029/92GL01802

Hartinger, M., Angelopoulos, V., Moldwin, M. B., Nishimura, Y., Turner, D. L., Glassmeier, K. H., & Stolle, C. (2012). Observations of a Pc5 global (cavity/waveguide) mode outside the plasmasphere by THEMIS. *Journal of Geophysical Research*, *117*, 6202. https://doi.org/10.1029/2011JA017266

Hartinger, M. D., Angelopoulos, V., Moldwin, M. B., Takahashi, K., & Clausen, L. B. N. (2013). Statistical study of global modes outside the plasmasphere. *Journal of Geophysical Research: Space Physics*, *118*, 804–822. https://doi.org/10.1002/jgra.50140

Hartinger, M. D., Welling, D., Viall, N. M., Moldwin, M. B., & Ridley, A. (2014). The effect of magnetopause motion on fast mode resonance. *Journal of Geophysical Research: Space Physics*, *119*, 8212–8227. https://doi.org/10.1002/2014JA020401

Inhester, B. (1987). Numerical modeling of hydromagnetic wave coupling in the magnetosphere. *Journal of Geophysical Research*, *92*, 4751–4756. https://doi.org/10.1029/JA092iA05p04751

Jacobs, J. A., Kato, Y., Matsushita, S., & Troitskaya, V. A. (1964). Classification of geomagnetic micropulsations. *Journal of Geophysical Research*, *69*, 180–181. https://doi.org/10.1029/JZ069i001p00180

Kivelson, M. G., & Southwood, D. J. (1985). Resonant ULF waves—A new interpretation. *Geophysical Research Letters*, *12*, 49–52. https://doi.org/10.1029/GL012i001p00049

Kivelson, M. G., & Southwood, D. J. (1986). Coupling of global magnetospheric MHD eigenmodes to field line resonances. *Journal of Geophysical Research*, *91*, 4345–4351. https://doi.org/10.1029/JA091iA04p04345

Klimushkin, D., Mager, P., & Glassmeier, K. (2004). Toroidal and poloidal Alfvén waves with arbitrary azimuthal wavenumbers in a finite pressure plasma in the Earth's magnetosphere. *Annales Geophysicae*, *22*, 267–287. https://doi.org/10.5194/angeo-22-267-2004

Lee, D. H., & Lysak, R. L. (1989). Magnetospheric ULF wave coupling in the dipole model—The impulsive excitation. *Journal of Geophysical Research*, *94*, 17,097–17,103. https://doi.org/10.1029/JA094iA12p17097

Lee, D. H., & Lysak, R. L. (1990). Effects of azimuthal asymmetry on ULF waves in the dipole magnetosphere. *Geophysical Research Letters*, *17*, 53–56. https://doi.org/10.1029/GL017i001p00053

Leonovich, A. S. (2001). A theory of field line resonance in a dipole-like axisymmetric magnetosphere. *Journal of Geophysical Research*, *106*, 25,803–25,812. https://doi.org/10.1029/2001JA000104

Leonovich, A. S., & Mazur, V. A. (1989). Resonance excitation of standing Alfven waves in an axisymmetric magnetosphere. I - Monochromatic oscillations. II—Nonstationary oscillations. *Planetary and Space Science*, *37*, 1095–1116. https://doi.org/10.1016/0032-0633(89)90081-0

Leonovich, A. S., & Mazur, V. A. (2000). Structure of magnetosonic eigenoscillations of an axisymmetric magnetosphere. *Journal of Geophysical Research*, *105*, 27,707–27,716. https://doi.org/10.1029/2000JA900108

Leonovich, A. S., & Mazur, V. A. (2001). On the spectrum of magnetosonic eigenoscillations of an axisymmetric magnetosphere. *Journal of Geophysical Research*, *106*, 3919–3928. https://doi.org/10.1029/2000JA000228

Mazur, V. A., & Chuiko, D. A. (2015). Azimuthal inhomogeneity in the MHD waveguide in the outer magnetosphere. *Journal of Geophysical Research: Space Physics*, *120*, 4641–4655. https://doi.org/10.1002/2014JA020819

Plaschke, F., Karlsson, T., Hietala, H., Archer, M., Vörös, Z., Nakamura, R., & Giles, B. L. (2017). Magnetosheath high-speed jets: Internal structure and interaction with ambient plasma. *Journal of Geophysical Research: Space Physics*, *122*, 10,157–10,175. https://doi.org/10.1002/2017JA024471

Rae, I. J., Donovan, E. F., Mann, I. R., Fenrich, F. R., Watt, C. E. J., Milling, D. K., & Balogh, A. (2005). Evolution and characteristics of global Pc5 ULF waves during a high solar wind speed interval. *Journal of Geophysical Research*, *110*, A12211. https://doi.org/10.1029/2005JA011007

Rickard, G. J., & Wright, A. N. (1994). Alfvén resonance excitation and fast wave propagation in magnetospheric waveguides. *Journal of Geophysical Research*, *99*, 13,455–13,464. https://doi.org/10.1029/94JA00674

Samson, J. C., Harrold, B. G., Ruohoniemi, J. M., Greenwald, R. A., & Walker, A. D. M. (1992). Field line resonances associated with MHD waveguides in the magnetosphere. *Geophysical Research Letters*, *19*, 441–444. https://doi.org/10.1029/92GL00116

Sandhu, J. K., Yeoman, T. K., Rae, I. J., Fear, R. C., & Dandouras, I. (2017). The dependence of magnetospheric plasma mass loading on geomagnetic activity using Cluster. *Journal of Geophysical Research: Space Physics*, *122*, 9371–9395. https://doi.org/10.1002/2017JA024171

Shen, X. C., Shi, Q., Wang, B., Zhang, H., Hudson, M. K., Nishimura, Y., & Degeling, A. W. (2018). Dayside magnetospheric and ionospheric responses to a foreshock transient on 25 June 2008: 1. FLR observed by satellite and ground-based magnetometers. *Journal of Geophysical Research: Space Physics*, *123*, 6335–6346. https://doi.org/10.1029/2018JA025349

Southwood, D. J. (1974). Some features of field line resonances in the magnetosphere. *Planetary Space Science*, *22*, 483–491. https://doi.org/10.1016/0032-0633(74)90078-6

Walker, A. D. M., Ruohoniemi, J. M., Baker, K. B., Greenwald, R. A., & Samson, J. C. (1992). Spatial and temporal behavior of ULF pulsations observed by the Goose Bay HF radar. *Journal of Geophysical Research*, *97*, 12,187–12,202. https://doi.org/10.1029/92JA00329

Wang, B., Nishimura, Y., Hietala, H., Shen, X. C., Shi, Q., Zhang, H., & Weatherwax, A. (2018). Dayside magnetospheric and ionospheric responses to a foreshock transient on 25 June 2008: 2. 2-D evolution based on dayside auroral imaging. *Journal of Geophysical Research: Space Physics*, *123*, 6347–6359. https://doi.org/10.1029/2017JA024846

Wright, A. N. (1994). Dispersion and wave coupling in inhomogeneous MHD waveguides. *Journal of Geophysical Research*, *99*, 159–167. https://doi.org/10.1029/93JA02206

Wright, A. N., & Elsden, T. (2016). The theoretical foundation of 3D Alfvén resonances: Normal modes. *Astrophysical Journal*, *833*, 230. https://doi.org/10.3847/1538-4357/833/2/230

Wright, A. N., Elsden, T., & Takahashi, K. (2018). Modeling the dawn/dusk asymmetry of field line resonances. *Journal of Geophysical Research: Space Physics*, *123*, 6443–6456. https://doi.org/10.1029/2018JA025638

Wright, A. N., & Rickard, G. J. (1995). A numerical study of resonant absorption in a magnetohydrodynamic cavity driven by a broadband spectrum. *Astrophysical Journal*, *444*, 458–470. https://doi.org/10.1086/175620

Zalesak, S. T. (1979). Fully multidimensional flux-corrected transport algorithms for fluids. *Journal of Computational Physics*, *31*, 335–362. https://doi.org/10.1016/0021-9991(79)90051-2